

# Deformation Mechanics of Self-expanding Venous Stents: Modelling and Experiments

Masoud Hejazi<sup>a</sup>, Farrokh Sassani<sup>a</sup>, J el Gagnon<sup>b</sup>, York Hsiang<sup>b</sup>, A. Srikantha Phani<sup>a,\*</sup>

<sup>a</sup>*Department of Mechanical Engineering, 6250 Applied Science Lane, University of British Columbia, Vancouver, B.C, Canada V6T 1Z4*

<sup>b</sup>*Division of Vascular Surgery, 4219-2775 Laurel Street, Vancouver General Hospital, Vancouver, B.C, Canada V5Z 1M9*

---

## Abstract

Deformation properties of venous stents based on braided design, chevron design, Z design, and diamond design are compared using *in vitro* experiments coupled with analytical and finite element modelling. Their suitability for deployment in different clinical contexts is assessed based on their deformation characteristics. Self-expanding stainless steel stents possess superior collapse resistance compared to Nitinol stents. Consequently, they may be more reliable to treat diseases like May-Thurner syndrome in which resistance against a concentrated (pinching) force applied on the stent is needed to prevent collapse. Braided design applies a larger radial pressure particularly for vessels of diameter smaller than 75% of its nominal diameter, making it suitable for a long lesion with high recoil. Z design has the least foreshortening, which aids in accurate deployment. Nitinol stents are more compliant than their stainless steel counterparts, which indicates their suitability in veins. The semi-analytical method presented can aid in rapid assessment of topology governed deformation characteristics of stents and their design optimization.

*Keywords:* Venous Stents, Foreshortening, Radial Pressure, Collapse

Manuscript word count: 3500

---

\*Corresponding author  
phone: +1 (604) 822-6998)  
fax: +1 (604) 822-2403  
email: srikanth@mech.ubc.ca

---

## 1. Introduction

Venous obstruction is a common pathological condition of the lower extremities, which reduces the vessel patency and hence the blood flow. Venous obstruction can be a result of a non-thrombotic syndrome (like May-Thurner and venous insufficiency) or an acute/chronic venous thrombosis (Murphy et al., 2017; Beebe-Dimmer et al., 2005). The prevalence and incidence rates of the venous obstruction vary depending on the underlying medical conditions. For instance, deep vein thrombosis (DVT) affects 300,000 people in North America each year with an incidence rate of 0.201% (Cohen et al., 2007; Silverstein et al., 1998; Arshad et al., 2017). Also, the prevalence rate of May-Thurner and chronic venous insufficiency are  $< 40\%$  and  $< 73\%$ , respectively (Cavalcante et al., 2015; Beebe-Dimmer et al., 2005; Radaideh et al., 2019). Some recent studies support endovascular treatment (stenting) over medical/compressive therapy (Rossi et al., 2018).

Vascular stents are small mesh-like porous tubular scaffolds, which are deployed inside diseased blood vessels to restore patency. These devices are available in various sizes, structures, and materials to provide desired mechanical properties in each particular design. Self-expanding and balloon-expandable stents are two major categories; each has a specific deployment procedure and expansion mechanism resulting in a different clinical performance. Since the balloon-expandable stents have a small range of elastic expansion, their self-expanding counterparts are preferred for deployment in veins because of their higher compliance and the ability to retain patency during the physiological dilation of veins (Wittens et al., 2015). Venous stenting evolved from the endovascular treatment of occlusive arteries. While the etiology of arterial and venous disease is different, arterial stents have been commonly used in off-label applications in venous endovascular treatment. However, recent studies on venous stenting suggested the need for designing venous stents accounting for the specific venous pathology (Schwein et al., 2018; Bento et al., 2019). The design

and manufacturing of venous stents have been overlooked and undervalued (Gordon et al., 2008) given the prevalence of venous disease and the off-label use of arterial stents. The main goal of this study is to examine stent deformation characteristics that contribute to their clinical performance and hence aid in the selection of a stent in a given clinical application.

Although atherosclerosis is the main etiology for the arteries, a chronic venous disease occurs due to venous thrombosis and external compression by the adjacent artery (Bento et al., 2019). Compared to arteries, veins are up to three times more compliant (distensible). Pathological arteries usually retain a well-defined vessel with almost no change in the vessel elasticity (Schwein et al., 2018). However, a pathological vein can undergo a fibrous retraction reducing its compliance. During the early stages of thrombosis, the venous thrombus is compliant and differentiable from the venous wall. During the chronic phase, 23 – 60% of acute DVT cases, the fibrotic thrombus is attached to the wall causing vein thickening and post-thrombotic recoil (Razavi et al., 2015; Deatrck et al., 2011). In summary, in designing a venous stent, one should consider the localized pinching forces (May-Thurner), high recoil (fibrotic veins), foreshortening (reduction of the length during expansion), and the large distensibility (high compliance) of the healthy wall proximal and distal to the pathological region. We first review pertinent literature on the deformation properties of stents.

The effect of radial pressure on the hemodynamics of a stented vessel has been investigated through experimental and computational studies (Freeman et al., 2010; Bedoya et al., 2006; Lally et al., 2005; Zahedmanesh and Lally, 2009). It is shown that a stent with excessive radial pressure constrains the cyclic dilation of the vessel leading to post-deployment complications such as restenosis (Morrow et al., 2005; Vernhet et al., 2001). Nevertheless, an optimal radial pressure is required to avoid post-deployment recoil and migration (Li and Kleinstreuer, 2006). The radial pressure is a function of stent structural parameters and the material properties, which has been extensively studied for braided stents (Zaccaria et al., 2020; Kim et al., 2008), Z stents (Snowhill et al.,

2001), and closed-cell venous stents (Dabir et al., 2018). In venous stenting, oversizing the stent is a common technique to avoid recoil and migration. Here we provide a semi-analytical method, in Section 3, to determine the radial pressure variation due to stent oversizing.

Collapse is a common failure mode for stents that are placed in veins (Murphy et al., 2017). Three different buckling modes in the collapse of balloon-expandable stents are identified in (Dumoulin and Cochelin, 2000) identified and collapse in self-expanding stents has been reported in (Kim et al., 2008; Dabir et al., 2018; Schwein et al., 2018). They observed mechanical instability by applying a pinching force on the stent structure. It has been reported that the local collapse stiffness of a stent depends critically on its strut geometry and the elastic modulus of the stent material (Duerig et al., 2000). We evaluate the performance of a venous stent against collapse experimentally and explain how we can qualitatively compare a stent's behavior under collapse through a unit-cell study.

Compliance of a stent also plays a vital role in its clinical performance particularly for the venous system with high distensibility. The stent is deployed to maintain adequate contact with the healthy wall proximally and distally in order to increase the anchoring area and avoid migration. The compliance mismatch between the vessel and the stent magnifies the post-deployment complications (Berry et al., 2002; Morris et al., 2016; Post et al., 2019). The compliance of a stent/vessel is defined as the variation of pressure over the variation of diameter. Here, the stent compliance is determined through experiment and analysis.

Despite the critical role of the foreshortening in precise stent placement, there is little study on the foreshortening of venous stents. For balloon-expandable arterial stents, however, the significance of longitudinal strain and the foreshortening mechanism has been elaborated in the literature (Douglas et al., 2014; Tan et al., 2011). However, the method cannot be used here due to differences in the expansion mechanism of self-expanding stents. Here, we measure the foreshortening during stent expansion and analytically study this parameter in Section

3.

The above studies confirm the importance of mechanical properties and deformation characteristics on the clinical performance of venous stents and a need to develop rapid assessment tools to inform the choice of stent topologies. Deformation characteristics of venous stents based on braided design, chevron design, Z design, and diamond design are compared using *in vitro* experiments coupled with analytical and finite element modelling. Their suitability for deployment in different clinical contexts is assessed based on their deformation characteristics. We start with an *in vitro* experiment to evaluate these parameters in Section 2. Afterwards, we employ the unit-cell study in Section 3 to determine radial pressure, compliance, foreshortening and collapse of the candidate stents in this study. We assess the validity of the unit-cell study by comparing the results with observations from the *in vitro* experiment and discuss clinical relevance in Sections 4 and 5. Concluding remarks and future work are given in Section 6.

## 2. *In vitro* experiments

Self-expanding stents are available in different structural design and materials. Here we chose two stainless steel stents (Z design and Braided design) and two Nitinol stents (Diamond design, Chevron design) shown in Fig. 1. Note that these stents are commercial designs currently being used in practice for venous stenting and here we use the design names instead of commercial names provided by companies. Among these, Braided design is the only one with an open-cell structure and the rest are closed-cell designs. Diamond design and Chevron design are the recent designs dedicated to venous stenting, Braided design is a common off-labeled design (used for both arteries and veins), and Z design is a trachea stent commonly used for venous stenting as a local reinforcement (Murphy et al., 2017). To study the effect of the material and structural design, we start with a series of *in vitro* tests to determine the radial pressure, collapse resistance, and foreshortening. Compliance, defined as the diameter variation ratio to radial pressure can be calculated as well.

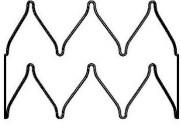
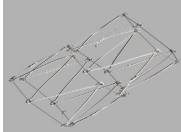
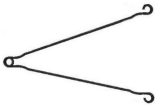
| Stent Design   | Stent Structure  | Unit-cell Geometry  | Strut Thickness (mm) | Strut Length ( $L_s$ ) (mm) | Material Volume/Length (mm <sup>3</sup> /mm) |
|----------------|--|---|----------------------|-----------------------------|--|
| Chevron design |   |  | 0.22                 | 8.0                         | 0.43   |
| Diamond design |   |  | 0.22                 | 5.1                         | 0.58   |
| Z design       |   |  | 0.34                 | 30.24                       | 0.94   |
| Braided design |  | NA  | 0.33                 | NA                          | 1.03   |

Figure 1: Stent designs used in this study and their structural design parameters.

The experimental setup for the *in vitro* tests are shown in Fig. 2. An environmental chamber was used to maintain the ambient temperature at 37° centigrade to simulate the body temperature. The radial pressure (i.e., circumferential resistive pressure) measured by the radial crimping test according to (Morris et al., 2016; Duda et al., 2000) shown in Fig. 2(a). An aluminum fabric of width equal to the undeployed length of the stent is wrapped around the fully deployed stent and threaded through a narrow gap between two rollers (diameter of 3 mm). The lower edge of the fabric is attached to the fixed jaw while the upper edge is attached to the moving jaw and the load cell. As the upper jaw moves upward, the circumference of the aluminum wrap decreases leading to reduction of the internal diameter and radial crimping of the stent. Note that in this case we only measure the circumferential resistive force, not

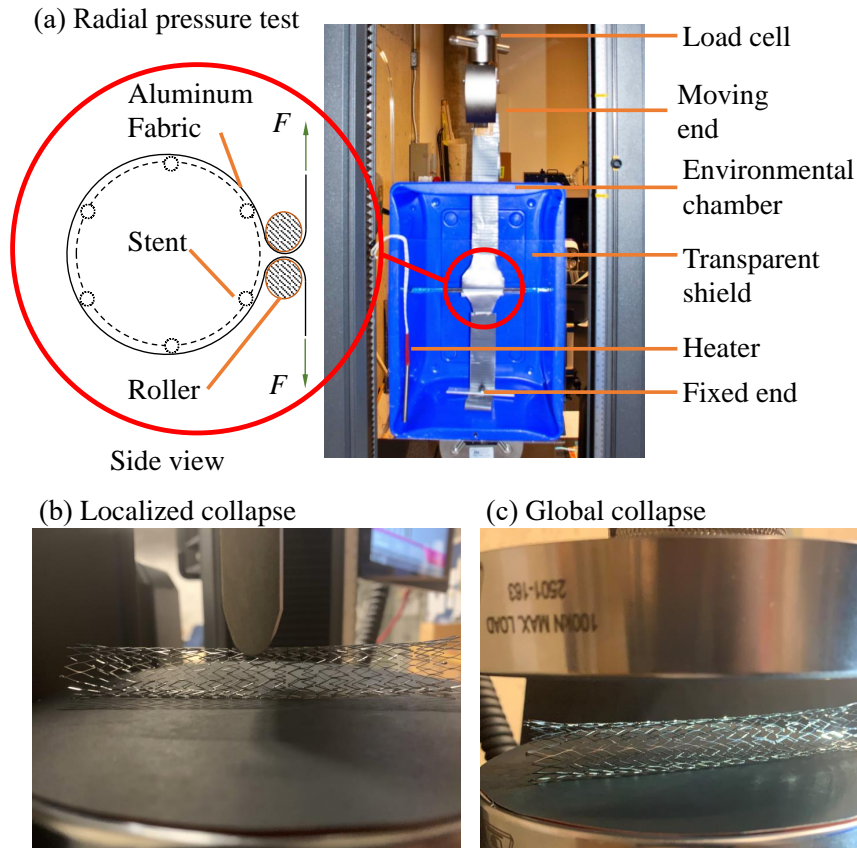


Figure 2: *In vitro* tests. (a) Stent is wrapped in an aluminum fabric sheet that is attached to the material testing machine (Instron 5965) grips at both ends. The rollers reduce the friction while the upper grip pulls the fabric and reduces the internal diameter of the aluminum warp. (b) The anvil applies compression locally at the mid-section of the stent. (c) The stent is globally compressed between two steel compression plates.

the chronic outward force that is applied by the stent to the wall during deployment. This is due to the fact that increasing the patency is commonly performed by immediate angioplasty after venous stenting. Hence, even if the chronic outward pressure is not enough, the angioplasty using balloon expansion can assist during deployment. Accordingly, the circumferential resistive force, resisting the post-deployment recoil, is a more representative characteristic in terms of clinical durability. In a temperature control chamber, the global

collapse and local collapse tests, based on the deformation modes suggested by (Dumoulin and Cochelin, 2000; Bandyopadhyay and Bose, 2013), were performed by compressing the stent by rigid plates and an anvil (tip diameter of 10 mm), respectively (See Fig. 2(a) and b). Results from the experiments will be presented and compared with semi-analytical model in Sections 4 and 5.

### 3. Unit-cell study and finite element analysis

The deformation characteristics of a stent rely on its lattice expansion mechanism, which can be investigated through a unit-cell study. This method can reduce the computation time and cost since the entire stent is not modelled. First, we start with defining the unit-cell for each design (see Fig. 3), where a cylindrical polar co-ordinate system ( $r - \theta - z$ ) is introduced in Fig. 3(a). The forces and moments associated with these co-ordinate axes are  $F_r$ ,  $F_\theta$  and  $M_z$ ,  $M_\theta$ , respectively. Each stent has  $n_a$  number of unitcells along the axial ( $z$ ) direction and  $n_c$  number of unitcells in the circumferential ( $\theta$ ) direction. Assuming periodic boundary conditions and axisymmetry of the structure, we can identify a unit-cell and define the boundary conditions at the decoupled joints/links as shown in Fig. 3(c). For uniform expansion and axisymmetric boundary conditions, the force  $F_r$ , and the moments  $M_\theta$ , and  $M_z$  can be neglected (Hejazi, 2018). Since Braided design is made through braiding, we cannot define a closed-joint uni-cell. Consequently, the approach to study the expansion of this stent will be different and discussed separately.

The venous pressure distribution acting on the stent is assumed to be uniform. Consequently, the resultant force  $F_p$  due to pressure, which is applied by vessel on all struts, acts at the center of the unit-cell in a radial direction and it is related to  $F_\theta$  (the tangential force applied to the joints) as:

$$F_p = 2F_\theta \sin \beta, \quad \beta = \frac{\pi}{n_c}. \quad (1)$$

We can define the length ( $L$ ) and the diameter ( $D$ ) of an expanding stent at each stage of deployment by following the method introduced by (Douglas et al.,

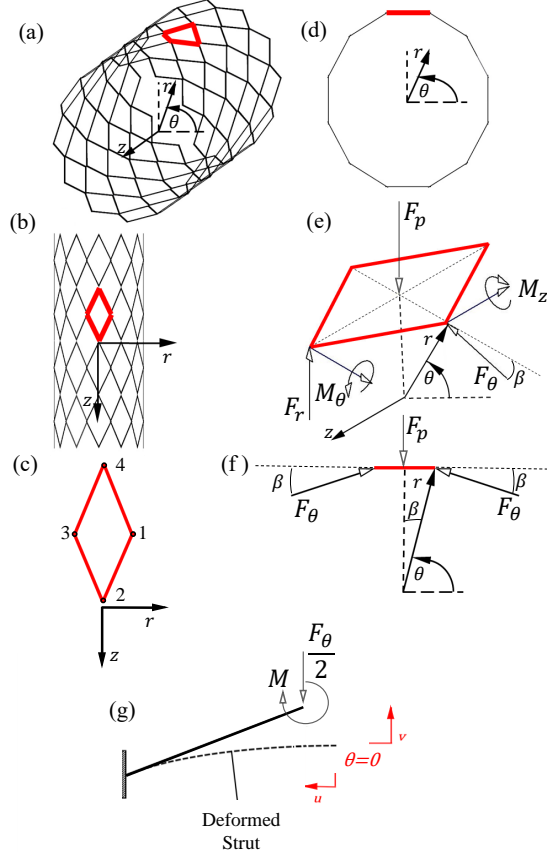


Figure 3: Typical geometry and loading conditions of a unit-cell in a stent structure. (a) cylindrical coordinate system; (b) top view of the isolated (highlighted) unit-cell in the structure; (c) four isolated joints of the unit-cell; (d) front view of the isolated unit-cell in the structure; (e) the reaction moments and forces applied to the isolated joints,  $F_p$  (resultant force due to contact pressure applied by the vessel to the stent),  $M_z$  and  $M_\theta$  (the reaction moment along  $z$  axis and  $\theta$  axis),  $F_r$  and  $F_\theta$  (the reaction forces along  $r$  axis and  $\theta$  axis); (f) the front view of a unit-cell loading condition; (g) kinematic role of a strut in deformation of a stent unit-cell. Each stent has  $n_a$  number of unitcells along the axial ( $z$ ) direction and  $n_c$  number of unitcells in the circumferential ( $\theta$ ) direction.

2014) below:

$$L = n_a(l_0 - 2u), \quad (2)$$

$$D = \frac{n_c(w_0 + 2v)}{\pi}, \quad (3)$$

where  $u, v, l_0$ , and  $w_0$  are respectively axial displacement, circumferential displacement, undeformed length, and width of a unit-cell (Fig. 3(g)). Note that for an unexpanded stent  $u = v = 0$  so that  $L = n_a l_0$  and  $D = \frac{n_c w_0}{\pi}$  define the initial length and diameter, respectively.

The main purpose of deploying a stent is to maintain the patency of the lumen. A vessel that tends to recoil applies a radial pressure to the stent, which governs post-deployment performance (Duerig et al., 2000; Morlacchi and Migliavacca, 2013). This pressure can be defined as:

$$P = \frac{F_p}{D\beta(l_0 - 2u)}, \quad (4)$$

Where  $P$  is the lumen radial pressure (circumferential resistive pressure), the numerator is the total applied force, and the denominator is the circumferential area of a unit-cell. By substituting (1), and (3) into (4) we have:

$$P = \frac{2F_\theta \sin\left(\frac{\pi}{n_c}\right)}{(w_0 + 2v)(l_0 - 2u)}. \quad (5)$$

We introduce the foreshortening parameter ( $f$ ) as

$$f = \frac{l_0 - l}{l_0} = \frac{2u}{l_0}, \quad (6)$$

where  $l = l_0 - 2u$  is the length of the unit-cell at a given stage of deployment. Using (6), we can rewrite the radial pressure as a function of foreshortening as follows:

$$P = \frac{2F_\theta \tan\left(\frac{\pi}{n_c}\right)}{(w_0 - 2v)l_0(1 + f)}. \quad (7)$$

The above indicates that  $P$  and  $f$  are inversely related. This suggests that while a large value of foreshortening is undesirable for precise deployment a larger radial pressure can be achieved. It is worth noting that this compromise in clinical performance can be avoided by choosing zero foreshortening stent-designs proposed in Douglas et al. (2014)

Compliance of a stent is defined according to

$$C = \frac{D_2 - D_1}{D_1(P_2 - P_1)}, \quad (8)$$

where  $D_i$  and  $P_i$  are the incremental stent diameter and pressure. By substituting equations (2) and (3) into (8), we have

$$C = \frac{v_1 - v_2}{\sin\left(\frac{\pi}{n_c}\right) \left( \frac{(w_0 + 2v_1)F_{\theta_2}}{(w_0 + 2v_2)(l_0 - 2u_2)} - \frac{F_{\theta_1}}{l_0 - 2u_1} \right)}. \quad (9)$$

Equations (2) to (9) indicate that for calculating the deformation characteristics (radial pressure, compliance, and foreshortening) we need to correlate the strut bending force ( $F_\theta$ ) with displacements in the circumferential ( $v$ ) and longitudinal ( $u$ ) directions. In Sections 3.1 and 3.2 we study the bending mechanism of the candidate stents, which governs the deformation characteristics of the stent.

### 3.1. Unit-cell deformation characteristics of Chevron design and Diamond design

Chevron design and Diamond stent designs used in this study are made of Nitinol alloy, which provides the desired mechanical properties such as superelasticity. The Nitinol struts undergo phase transition depending on the mechanical strain which influences their deformation characteristics. A mathematical model is introduced for the bending analysis of Nitinol beams in (Mirzaeifar et al., 2013). We apply their model to find the deformation of the stent strut subjected to bending described in Fig. 3(g). The bending analysis for a cantilever beam is summarized in Appendix A1. The Chevron design has a more complex shape, which can be divided into curved and straight sections (Fig. 4). Hence, we have to modify (5), (6), (7), and (9) by substituting circumferential displacement  $v$  by  $3v$  and longitudinal displacement  $u$  by  $0.5u$  to account for the number of struts in the unit-cell and the different orientation of the joints. We can use equations (10) and (11) respectively, to calculate the bending moment in the curved and straight portion as:

$$M_c = \frac{1}{2}Fl \cos \alpha - Fr(1 - \cos \theta), \quad (10)$$

$$M_l = \frac{1}{2}Fl \cos \alpha - Fx \cos \alpha + Fr. \quad (11)$$

where  $\theta$  and  $x$  locate the section in the curved and the straight part, respectively in Fig. 4(b) and in Fig. 4(d). Using (10) and (11) we can calculate the bending moment throughout the strut of Chevron design as a function of  $\theta$  for the curved portion and  $x$  for the straight part. In these equations,  $l$  is the effective arm length of the strut (contributing in bending moment),  $r$  is the radius of the curved portion, and  $F = F_\theta \cos \beta$  based on Fig. 4. For the Diamond stent (Nitinol) since there is no curved region at the intersection of joints, we can directly use the analysis of a cantilever beam in Appendix A1 to calculate the internal bending moments during deployment. Having thus found the internal forces we can calculate the deformation properties of these two designs by following the Appendix A1 to find the displacements and calculate radial pressure and compliance using (7) and (9) .

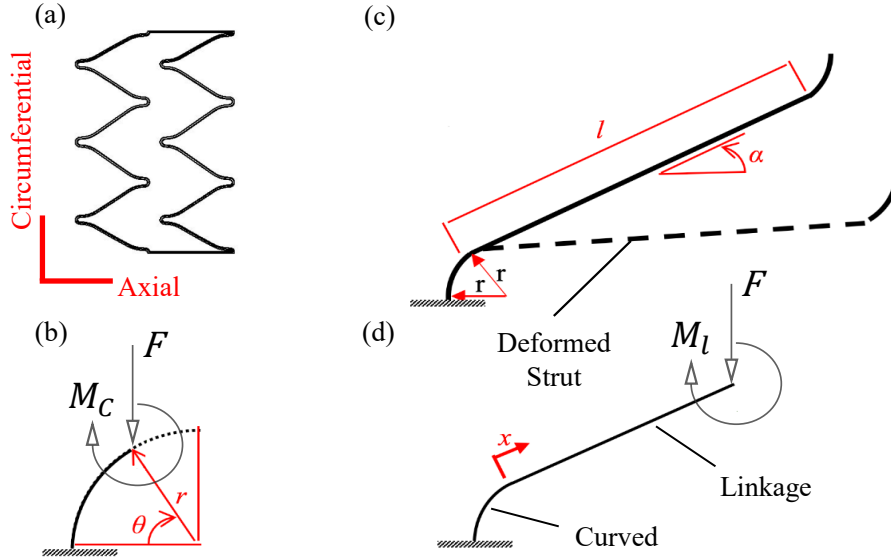


Figure 4: (a) Chevron design unit-cell geometry; (b) a strut of the unit-cell including the curved and linear parts; (c) the bending moment and shear force at a given cross section of the curve part; (d) the bending moment and shear force at a given cross section of the linkage.

### 3.2. Unit-cell deformation characteristics of Z design and Braided design

Geometric design imparts self-expanding ability to Z design and Braided design stents. Two sets of steel links and a coil that connect these links are the elements that define the Z design unit-cell. Accordingly, we can calculate the displacement of the strut based on the coil angular twist and the elastic bending of the link. The displacement in a single strut is a combination of the coil angular twist and the link bending deflection. The torsional stiffness ( $k_t$ ) of the coil and the torsion angle can be calculated through  $k_t = \frac{Ed^4}{10.8Dn}$ , where  $E, d, D, n$ , and  $l$  are torsional stiffness, Young's modulus, wire diameter, the diameter of the coil, number of coil body turns, the torsion angle and link length (Budynas et al., 2008). Accordingly, the angular twist of the coil part, longitudinal and circumferential displacements can be determined through

$$\gamma = k_t F(l + 2d), \quad (12)$$

$$u = l(1 - \cos \gamma), \quad (13)$$

$$v = \frac{Fl^3}{3EI} + l \sin \gamma. \quad (14)$$

In (12) we can determine the longitudinal displacement of the strut tip in terms of the angular twist. Here, we ignore the contribution of the strut bending as it is in the elastic region of the bending deformation and can be assumed small in comparison to the effect of an angular twist. To calculate the circumferential displacement, we can use (13), in which, the first term is the contribution of bending displacement and the second term represents the effect of coil angular twist.

Braided design is fabricated by braided wires forming its entire structure. Consequently, it does not have any true geometrical unit-cell or joint and therefore no real strut can be defined. The expansion of Braided design was investigated to derive an equation that relates the pressure to the diameter of the

Braided design structure based on slender bar theory (Wang and Ravi-Chandar, 2004a,b) as:

$$P = \frac{n \cos^2 \alpha}{2\pi r^2 \sin^2 \alpha} \left[ \begin{array}{l} \frac{EI \sin \alpha}{r} \left( \frac{\cos^2 \alpha}{r} - \frac{\cos^2 \alpha_0}{r_0} \right) \\ - \frac{GI_p \cos \alpha}{r} \left( \frac{\cos \alpha \sin \alpha}{r} - \frac{\cos \alpha_0 \sin \alpha_0}{r_0} \right) \end{array} \right], \quad (15)$$

$$f = \frac{\sqrt{\lambda_0^2 + 4\pi^2 r_0^2} - 4\pi^2 r^2 - \lambda_0}{\lambda_0}, \quad (16)$$

Where  $n, E, G, I_p, r,$  and  $r_0$  are respectively number of wires, Young's modulus, shear modulus, the area moment of inertia, stent radius, and nominal radius. To calculate the foreshortening, we can use (16), in which  $\lambda_0$  and  $r_0$  are initial helical wire pitch and diameter. Furthermore, to determine the compliance, instead of using (9), which has been used for other stents, we can directly use (8) associated with radial pressure values from (15).

### 3.3. Finite element simulation parameters and material properties

In this work, the simulation has been performed in ABAQUS/Standard commercial code linked with a user material subroutine (UMAT) based on (Lagoudas, 2008). Here, the FE method was employed to evaluate two different problems. We studied the bending of the Chevron design and Diamond design struts to validate the method presented in (Mirzaeifar et al., 2013), which addresses the bending mechanics of a Nitinol beam. We used material properties of NITI-I for Nitinol stents, and an elastic modulus of 193 GPa, Poisson's ratio of 0.3 and uniaxial yield stress of 260 MPa for steel stents (Bandyopadhyay and Bose, 2013; Duerig et al., 2000). We employed UMAT (user material subroutine), which is a framework for ABAQUS users to implement a material (Nitinol model was not available in the software library at the time of this study). The foundation of the UMAT code is the thermo-mechanical constitutive model of Nitinol (Auricchio and Taylor, 1997; Bhattacharya, 2003; Lagoudas, 2008). We used fully integrated solid linear hexahedron element (C3D20) for other designs. The global size for the meshing varies from 0.075 mm to 0.05 mm based on the mesh

sensitivity test. The numerical finite element results are used to validate the semi-analytical method for bending of Nitinol struts, presented in Section 3.1.

#### 4. Results

A comparison is drawn between FE simulation (Section 3.2) and the semi-analytical approach (Section 3.1) results for a strut bending of the Nitinol stents in Fig. 5. The change of the slope reflects the onset of phase transition (austenite to martensite). The FE solution here is stiffer for Chevron design. For Diamond design, however, the semi-analytical method demonstrated a stiffer response. This is because of the shear stress contribution to the phase transition, which has been ignored in Section 3.1. The change of the slope reflects the onset of phase transition (austenite to martensite). If von Mises stress is more than 260 MPa, the region has a pure martensite phase. A core of pure austenite always exists for the Chevron design joints. For Diamond design, however, we observe a core of martensite phase close to the joints.

The foreshortening of the stents, illustrated in Fig. 6, has been calculated through (6) for joint based designs (Z design, Diamond design, and Chevron design) and (16) for Braided design. It should be noted that the foreshortening is a dimensionless characteristic and the presented results in Fig. 6 are valid for different stent sizes. As shown, in all cases the experimental values of foreshortening is smaller. This can be the result of longitudinal compressive forces (due to the friction) that is applied to the stent during the crimping test in the aluminum fabric.

In clinical practice, stents are oversized to maintain a required radial pressure. Fig. 7 shows the radial pressure versus the over-sizing parameter ( $D_n/D_v$ ), where  $D_n$  and  $D_v$  are stent nominal expanded diameter and vessel diameter, respectively. For a given  $D_n = 16mm$ , the experimental data points were measured through the *in vitro* test setup shown in Section 2. In this case, we simulate  $D_v$  by adjusting the diameter of the aluminum wrap. For each stent, the joint analysis (Sections 3.2 and 3.3) yields the circumferential force ( $F_\theta$ ) and

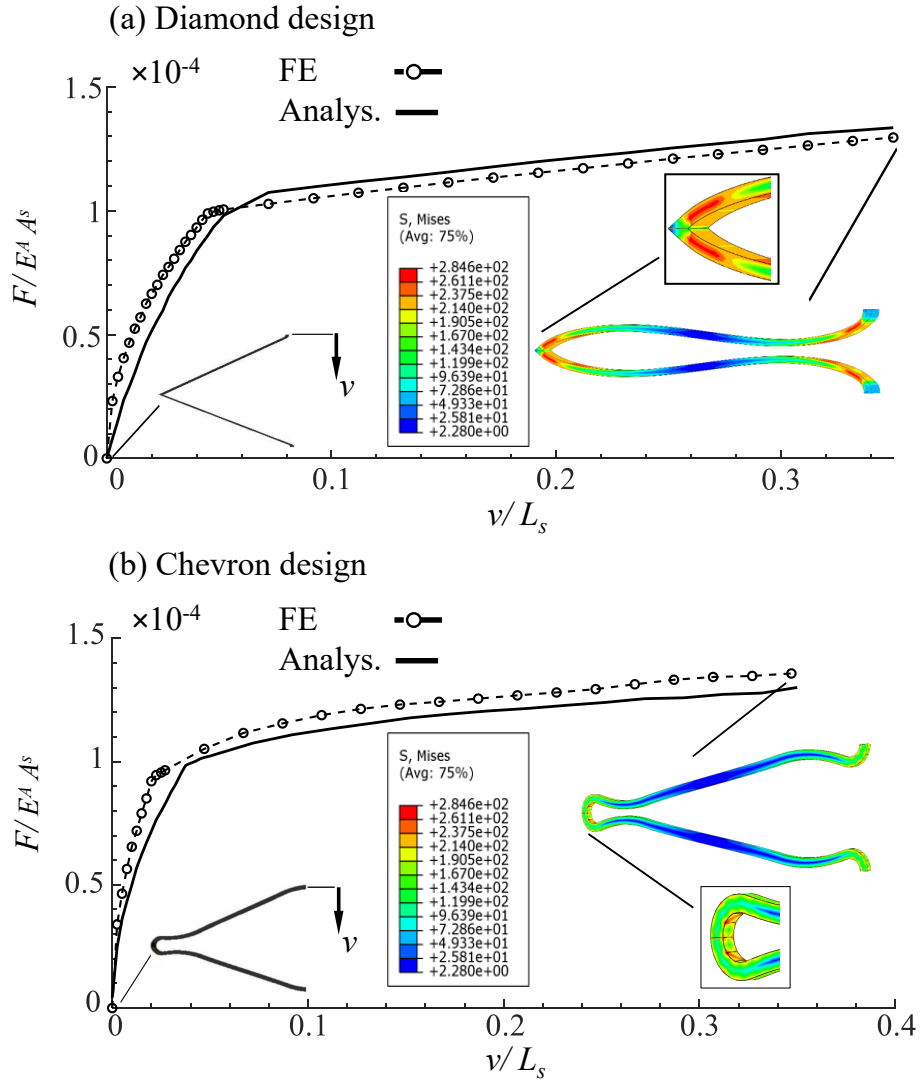


Figure 5: Von Mises stress distribution over the stent strut at the delivery size (maximum magnitude of stress); (a) Diamond design joint; (b) Chevron design. Comparison between strut bending force vs. circumferential displacement from the analytical method in Section 3 and Finite Element calculations.

longitudinal displacement ( $u$ ), at a given circumferential displacement ( $v$ ). In this case, circumferential displacement is adjusted to match the simulated vessel diameter using (3). Accordingly, (5) was used to calculate the radial pressure.

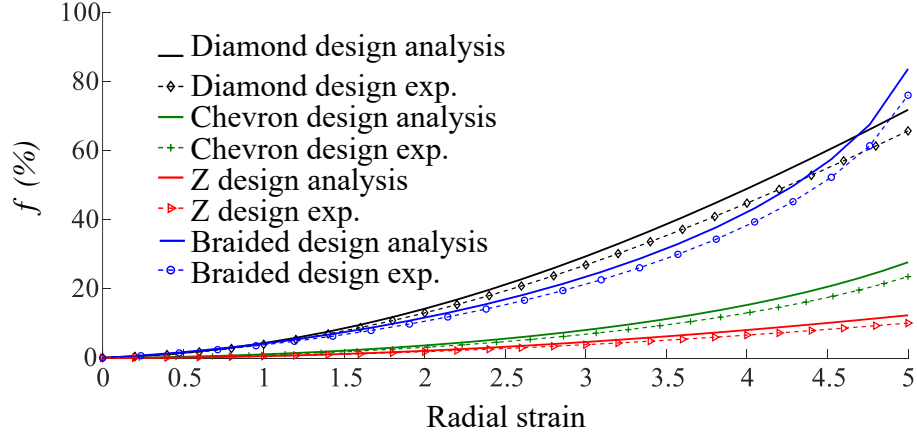


Figure 6: Analytical prediction of foreshortening compared with experimental measurements.

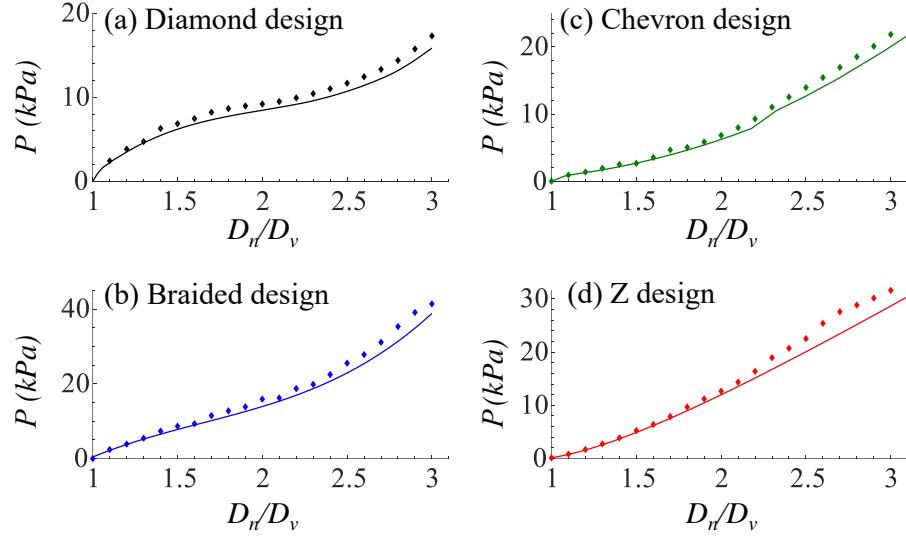


Figure 7: Radial pressure calculated based on (5), shown by solid line, compared with data points corresponding to *in vitro* experiment (Fig Fig. 2(a)).  $D_n$  and  $D_v$  are stent nominal expanded diameter and vessel diameter, respectively. Usually the ratio  $\frac{D_n}{D_v}$  does not exceed 1.3 which corresponds to 30% oversizing.

We can compare the radial pressure performance of the stents in Fig. 8(a), where we combine and compare all stents in Fig. 7 in a single plot for a better comparison. Note that the oversizing parameter is limited to  $D_n/D_v = 1.3$  since

30% oversizing is recommended in most of the clinical cases. Diamond design and Braided design have a larger radial pressure in this range. Although, Z design has the highest maximum radial pressure at  $D_n/D_v = 3$ , it loses 70% of its radial pressure at  $D_n/D_v = 1.5$ . To compare stent radial compliance, calculated using (8), we have Fig. 8(b). The steel stents (Braided design and Z design) are much more compliant at higher oversizing values. However, in the range of  $D_n/D_v < 1.5$ , they are much stiffer. The compliance of Nitinol stents, Chevron design and Diamond design, does not change as much as steel stents with changing the oversizing  $D_n/D_v$ . This can be due to the effect of the phase transition, which is evident in the local maximum points in the compliance curve.

The results of the global and local collapse tests are shown in Fig. 9(a) and (b), respectively. Wall stent and Z design have the higher resistance in both tests compared to Nitinol stents. Note that Z design has a higher resistance to localized collapse while Braided design performs better in global collapse test. It is worth mentioning that steel stents were also stiffer in the radial pressure test when  $D_n/D_v < 1.5$ .

## 5. Discussion

### 5.1. Results assessment, validation, and limitations

The assumption on loading conditions and resultant deformation of the semi-analytical method is validated through comparison with experiments (Fig. 7). The experiments show a slightly higher pressure, especially at higher expansion ratio ( $\frac{D_n}{D_v} > 1.3$ ). This is partly due to friction forces exerted by the wrapping foil used in experiments, and the loading-unloading hysteresis. Further, in the semi-analytical method pure bending is assumed and torsional loads are ignored as axi-symmetric deformation is assumed. The role of shear in the deflection of the strut accounts for a portion of error, particularly for Diamond design as we can see in Fig. 5, where FE predicts the phase transition at a smaller displacement. The curved part of the Chevron design structure is connected to

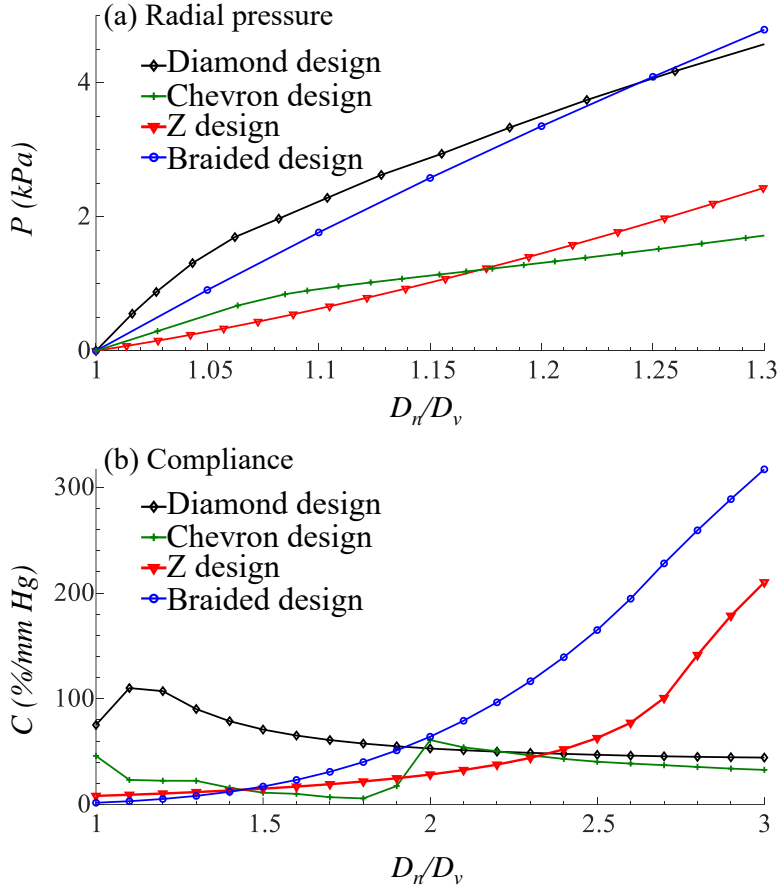


Figure 8: Experimental measurements of radial pressure and compliance of stents compared in a single plot.

the straight strut by another fillet curve. Since the connection between these parts is assumed as a straight link for the purpose of simplification, the results deviate from the experiments. This conclusion is also valid for the fillet that connects the curved and straight parts of the Z design (See Fig. 4).

In Fig. 8(a), we observe a higher radial pressure (up to 30% oversizing,  $D_n/D_v = 1.3$ ) for Diamond design and Braided design (steel stents). They offer more scaffolding than Z design and Chevron design (Nitinol stents) due to higher coverage. The radial pressure is a function of bending force in each unit-cell,

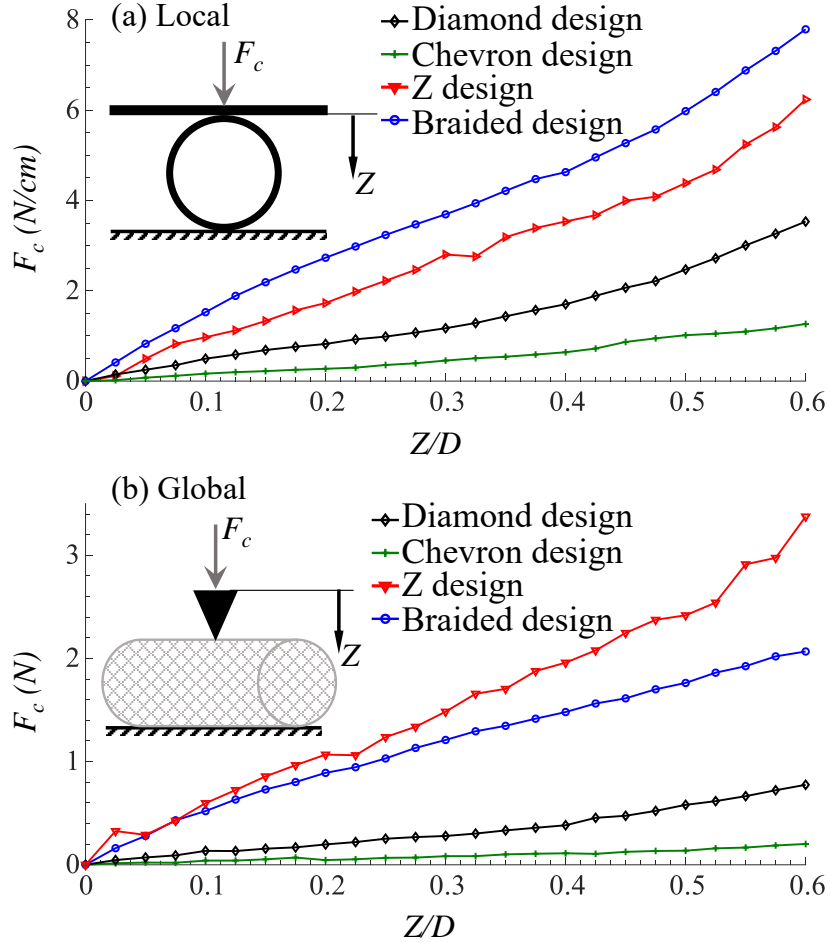


Figure 9: Experimental measurements of collapse force ( $F_c$ ) Vs. displacement ratio ( $Z/D$ ).  $D$  is the internal diameter of the fully expanded stent.

and the bending force itself is a function of the cross-section area, length of the strut, the material of the stent, and foreshortening according to (7). Hence, with higher foreshortening, the material volume per unit length increases and the total contact surface decreases, which leads to higher radial pressure. Another remarkable observation is the relationship between compliance and collapse resistance. By comparing Fig. 8(b) and Fig. 9, we can conclude that steel stents are less susceptible to collapse. Consequently, collapse resistance is inversely

correlated to compliance. When the collapse mode has a spatially non-uniform deformation as a result of structural instability the analytical method given here is not applicable. However, given the relationship between collapse resistance and radial compliance (calculated based on (9)), it is possible to qualitatively compare the collapse behavior of stent designs.

The limitation of the present study arises in both experimental and analytical modelling. The *in vitro* experiment based on Section 2 only considers the uniform deployment and does not account for non-uniform lumen or a curved anatomy of the vein. In general it is a challenge to excise fibrotic veins and the vein material properties are difficult to emulate using polymeric tubes. This means that the vein-stent interaction is not accounted in this study. This is an area where further work is needed. However, for a given vein model the relative performance that we report in this study is expected to hold. Another alternative approach to measure the radial pressure is to use an aperture-type (crimper) machine (see (Dabir et al., 2018; McKenna and Vaughan, 2020)). The limitations listed above are still unavoidable. Another consideration is the effect of foreshortening on the radial pressure test. In the setup used here, it is easy to use a wider fabric to account for stent elongation during the crimp test. In the aperture-type devices, however, the length of the stent is limited to the device capacity. In the analytical approach (Section 3), we ignored the frictional forces and the mechanical interaction between the vein wall and the stent was modelled as a uniform pressure distribution, which is not the case for curved vessel geometries. This effect can be included in future studies by assuming the elasticity of the vessel wall.

### 5.2. *Clinical significance*

This study compares four different venous stent designs (Chevron design, Z design, Diamond design, and Braided design) based on their collapse, foreshortening, radial pressure, and compliance. Usually, the stent deployment for abnormal/diseased vein is performed after the vein angioplasty under fluoroscopy. Consequently, a surgeon can observe the length of occlusion, the regions

with high forces (based on the shape of inflated balloon), and the stiffness of the occluded part by observing the balloon pressure. Based on the mechanical properties of the diseased vein, we can suggest the most suitable design for a specific occlusion type. Based on our study, here we present a summary of some of the common vein occlusion scenarios.

- Z design has superior performance against collapse deformation. Consequently, it may be more reliable to treat diseases like May-Thurner syndrome, which tends to apply localized force.
- Nitinol stents are more compliant. Thus they follow the joint movements. Accordingly, they are more suitable for deployment in proximity of expected major vessel bending during limbs movements. Diamond design and Braided design apply a higher radial pressure. Thus, they may be chosen for the long lesion with high recoil.
- Stents have a number of anchors at both ends, which attach them to the vessel wall to avoid migration. If the locations of the stent tips are critical to be predicted (e.g., deployment close to branch orifice), Z design can be a good choice. Because of the small foreshortening of Z design in comparison to other designs, we can predict the final location of the ends.

## 6. Conclusions

This study compared four different stents currently used in veins. Two designs (Z, braided stents) are off-label while the remaining two (Diamond and Chevron) are specifically designed for venous stenting. Deformation characteristics of all four designs are compared under identical loading conditions through *in -vivo* testing and semi-analytical modelling. Particular attention is given to foreshortening, compliance, radial pressure, and collapse resistance. An inverse correlation between radial compliance and collapse resistance, and foreshortening and radial pressure is found. A good agreement is found between the predictions of the unit cell based semi-analytical modelling and experiments.

Relative merits of each stent design for common vein occlusion scenarios are identified. Venous stenting is a relatively new area of investigation compared with arterial stents. While we expect the relative comparison across the designs to hold, further work on vein-stent interaction is needed.

### **Conflict of interest**

The authors claim no conflict of interest regarding the choice of candidate stents. No human or animal test was conducted for this study.

### **Acknowledgment**

We sincerely acknowledge the Division of Vascular Surgery at Vancouver General Hospital for providing the stent models. Furthermore, the funding through a Discovery Grant to Srikantha A. Phani from Natural Sciences and Engineering Research Council (NSERC) Canada is acknowledged.

### **References**

- Arshad, N., Isaksen, T., Hansen, J.B., Brækkan, S.K., 2017. Time trends in incidence rates of venous thromboembolism in a large cohort recruited from the general population. *European Journal of Epidemiology* 32, 299–305.
- Auricchio, F., Taylor, R.L., 1997. Shape-memory alloys: modelling and numerical simulations of the finite-strain superelastic behavior. *Computer Methods in Applied Mechanics and Engineering* 143, 175–194.
- Bandyopadhyay, A., Bose, S., 2013. *Characterization of biomaterials*. Elsevier, Amsterdam.
- Bedoya, J., Meyer, C.A., Timmins, L.H., Moreno, M.R., Moore, J.E., 2006. Effects of stent design parameters on normal artery wall mechanics. *Journal of Biomechanical Engineering* 128, 757–765.

- Beebe-Dimmer, J.L., Pfeifer, J.R., Engle, J.S., Schottenfeld, D., 2005. The epidemiology of chronic venous insufficiency and varicose veins. *Annals of Epidemiology* 15, 175–184.
- Bento, D., Machado, R., Mendes, D., Almeida, R.d., 2019. Tratamento endovascular da doença venosa crônica oclusiva-especificações das endoproteses e comparação de resultados. *Angiologia e Cirurgia Vascul* 15, 76–85.
- Berry, J.L., Manoach, E., Mekkaoui, C., Rolland, P.H., Moore Jr, J., Rachev, A., 2002. Hemodynamics and wall mechanics of a compliance matching stent: in vitro and in vivo analysis. *Journal of Vascular and Interventional Radiology* 13, 97–105.
- Bhattacharya, K., 2003. Microstructure of martensite: why it forms and how it gives rise to the shape-memory effect. volume 2. Oxford University Press, Oxford.
- Budynas, R.G., Nisbett, J.K., et al., 2008. Shigley’s mechanical engineering design. volume 8. McGraw-Hill, New York.
- Cavalcante, L.P., Souza, J.E.d.S., Pereira, R.M., Bernardes, M.V., Amanajás, A.M.d.S., Parisati, M.H., Rocha, R.D.d., Araújo, A.O.d., 2015. Iliac vein compression syndrome: literature review. *Jornal Vascular Brasileiro* 14, 78–83.
- Cohen, A.T., Agnelli, G., Anderson, F.A., Arcelus, J.I., Bergqvist, D., Brecht, J.G., Greer, I.A., Heit, J.A., Hutchinson, J.L., Kakkar, A.K., et al., 2007. Venous thromboembolism (VTE) in Europe. *Thrombosis and Haemostasis* 98, 756–764.
- Dabir, D., Feisst, A., Thomas, D., Luetkens, J.A., Meyer, C., Kardulovic, A., Menne, M., Steinseifer, U., Schild, H.H., Kuetting, D.L., 2018. Physical properties of venous stents: an experimental comparison. *Cardiovascular and Interventional Radiology* 41, 942–950.

- Deatrick, K.B., Elfline, M., Baker, N., Luke, C.E., Blackburn, S., Stabler, C., Wakefield, T.W., Henke, P.K., 2011. Postthrombotic vein wall remodeling: preliminary observations. *Journal of Vascular Surgery* 53, 139–146.
- Douglas, G.R., Phani, A.S., Gagnon, J., 2014. Analyses and design of expansion mechanisms of balloon expandable vascular stents. *Journal of Biomechanics* 47, 1438–1446.
- Duda, S.H., Wiskirchen, J., Tepe, G., Bitzer, M., Kaulich, T.W., Stoeckel, D., Claussen, C.D., 2000. Physical properties of endovascular stents: an experimental comparison. *Journal of Vascular and Interventional Radiology* 11, 645–654.
- Duerig, T., Tolomeo, D., Wholey, M., 2000. An overview of superelastic stent design. *Minimally Invasive Therapy and Allied Technologies* 9, 235–246.
- Dumoulin, C., Cochelin, B., 2000. Mechanical behaviour modelling of balloon-expandable stents. *Journal of Biomechanics* 33, 1461–1470.
- Freeman, J.W., Snowhill, P.B., Noshier, J.L., 2010. A link between stent radial forces and vascular wall remodeling: the discovery of an optimal stent radial force for minimal vessel restenosis. *Connective Tissue Research* 51, 314–326.
- Gordon, B.M., Fishbein, M.C., Levi, D.S., 2008. Polytetrafluoroethylene-covered stents in the venous and arterial system: angiographic and pathologic findings in a swine model. *Cardiovascular Pathology* 17, 206–211.
- Hejazi, M., 2018. A comparative assessment of deformation characteristics of self-expanding venous stents. Master’s thesis. University of British Columbia, Vancouver.
- Kim, J.H., Kang, T.J., Yu, W.R., 2008. Mechanical modeling of self-expandable stent fabricated using braiding technology. *Journal of Biomechanics* 41, 3202–3212.

- Lagoudas, D.C., 2008. Shape memory alloys: modeling and engineering applications. Springer Science and Business Media.
- Lally, C., Dolan, F., Prendergast, P., 2005. Cardiovascular stent design and vessel stresses: a finite element analysis. *Journal of Biomechanics* 38, 1574–1581.
- Li, Z., Kleinstreuer, C., 2006. Analysis of biomechanical factors affecting stent-graft migration in an abdominal aortic aneurysm model. *Journal of Biomechanics* 39, 2264–2273.
- McKenna, C.G., Vaughan, T.J., 2020. An experimental evaluation of the mechanics of bare and polymer-covered self-expanding wire braided stents. *Journal of the Mechanical Behavior of Biomedical Materials* 103, 103549.
- Mirzaeifar, R., DesRoches, R., Yavari, A., Gall, K., 2013. On superelastic bending of shape memory alloy beams. *International Journal of Solids and Structures* 50, 1664–1680.
- Morlacchi, S., Migliavacca, F., 2013. Modeling stented coronary arteries: where we are, where to go. *Annals of Biomedical Engineering* 41, 1428–1444.
- Morris, L., Stefanov, F., Hynes, N., Diethrich, E.B., Sultan, S., 2016. An experimental evaluation of device/arterial wall compliance mismatch for four stent-graft devices and a multi-layer flow modulator device for the treatment of abdominal aortic aneurysms. *European Journal of Vascular and Endovascular Surgery* 51, 44–55.
- Morrow, D., Sweeney, C., Birney, Y.A., Cummins, P.M., Walls, D., Redmond, E.M., Cahill, P.A., 2005. Cyclic strain inhibits notch receptor signaling in vascular smooth muscle cells in-vitro. *Circulation Research* 96, 567–575.
- Murphy, E.H., Johns, B., Varney, E., Buck, W., Jayaraj, A., Raju, S., 2017. Deep venous thrombosis associated with caval extension of iliac stents. *Journal of Vascular Surgery: Venous and Lymphatic Disorders* 5, 8–17.

- Post, A., Diaz-Rodriguez, P., Balouch, B., Paulsen, S., Wu, S., Miller, J., Hahn, M., Cosgriff-Hernandez, E., 2019. Elucidating the role of graft compliance mismatch on intimal hyperplasia using an ex vivo organ culture model. *Acta Biomaterialia* 89, 84–94.
- Radaideh, Q., Patel, N.M., Shamma, N.W., 2019. Iliac vein compression: epidemiology, diagnosis and treatment. *Vascular Health and Risk Management* 15, 115.
- Razavi, M.K., Jaff, M.R., Miller, L.E., 2015. Safety and effectiveness of stent placement for iliofemoral venous outflow obstruction: systematic review and meta-analysis. *Circulation: Cardiovascular Interventions* 8, e002772.
- Rossi, F.H., Kambara, A.M., Izukawa, N.M., Rodrigues, T.O., Rossi, C.B., Sousa, A.G., Metzger, P.B., Thorpe, P.E., 2018. Randomized double-blinded study comparing medical treatment versus iliac vein stenting in chronic venous disease. *Journal of Vascular Surgery: Venous and Lymphatic Disorders* 6, 183–191.
- Schwein, A., Georg, Y., Lejay, A., Nicolini, P., Hartung, O., Contassot, D., Thaveau, F., Heim, F., Chakfe, N., 2018. Endovascular treatment for venous diseases: where are the venous stents? *Methodist deBakey cardiovascular journal* 14, 208.
- Silverstein, M.D., Heit, J.A., Mohr, D.N., Petterson, T.M., O’Fallon, W.M., Melton, L.J., 1998. Trends in the incidence of deep vein thrombosis and pulmonary embolism: a 25-year population-based study. *Archives of Internal Medicine* 158, 585–593.
- Snowhill, P., Noshier, J., Siegel, R., Silver, F., 2001. Characterization of radial forces in z stents. *Investigative Radiology* 36, 521–530.
- Tan, T.W., Douglas, G.R., Bond, T., Phani, A.S., 2011. Compliance and longitudinal strain of cardiovascular stents: influence of cell geometry. *Journal of Medical Devices* 5.

- Vernhet, H., Demaria, R., Juan, J.M., Oliva-Lauraire, M.C., Senac, J.P., Dautzat, M., 2001. Changes in wall mechanics after endovascular stenting in the rabbit aorta: comparison of three stent designs. *American Journal of Roentgenology* 176, 803–807.
- Wang, R., Ravi-Chandar, K., 2004a. Mechanical response of a metallic aortic stent - part I: pressure-diameter relationship. *Journal of Applied Mechanics* 71, 697–705.
- Wang, R., Ravi-Chandar, K., 2004b. Mechanical response of a metallic aortic stent - part II: a beam-on-elastic foundation model. *Journal of Applied Mechanics* 71, 706–712.
- Wittens, C., Davies, N., Bwkgaard, N., Broholm, R., Cavezzi, A., Chastanet, S., De Wolf, M., Eggen, C., Giannoukas, A., Gohel, M., Kakkos, S., et al., 2015. Editor’s choice - management of chronic venous disease clinical practice guidelines of the European Society for Vascular Surgery (ESVS). *European Journal of Vascular and Endovascular Surgery* 49, 678–737.
- Zaccaria, A., Migliavacca, F., Pennati, G., Petrini, L., 2020. Modeling of braided stents: Comparison of geometry reconstruction and contact strategies. *Journal of biomechanics* , 109841.
- Zahedmanesh, H., Lally, C., 2009. Determination of the influence of stent strut thickness using the finite element method: implications for vascular injury and in-stent restenosis. *Medical and Biological Engineering and Computing* 47, 385–393.

#### **A1. Material properties and Elastic bending of Nitinol beams**

The correlation between elastic curvature ( $\kappa$ ) and the bending moment is given in (17), where  $y_{1c}$  and  $y_{2c}$  are respectively the distance from the neutral axis to the boundaries of the transition, and martensite regions, which are under compression (Fig. 10); the same terminology is true for  $y_{1t}$  and  $y_{2t}$  which are

representing the same variables for the tension portion. Thermo-mechanical properties for NITI-I are given in Table 1. To calculate  $I$  in (17), (Mirzaeifar et al., 2013) introduced four different functions for different loading conditions. Here, we used equation (24) in their paper. Accordingly, we determine the bending moment in each strut (a function of  $F_\theta$ ) and find the curvature of the stent strut based on the method presented by (Mirzaeifar et al., 2013). Once we have the curvature along the strut length, we can find the circumferential and longitudinal displacements.

$$\begin{aligned}
M(\kappa) = & -1/3E^A\kappa(y_{1c}^3 - y_{1t}^3) + (I(y_{2c}) - I(y_{1c})) + \\
& E^M w[1/3\kappa((h_c^3)/8 - y_{2c}^3) - H^c((h_c^2)/4 - y_{2c}^2)] + (I(y_{2t}) - I(y_{1t})) \\
& + E^M w[1/3\kappa(y_{2t}^3 - (h_t^3)/8) - H^c(y_{2t}^2 - (h_t^2)/4)], \quad (17)
\end{aligned}$$

Where  $y_{1c}, y_{2c}, y_{1t}$ , and  $y_{2t}$  are given in equations (32) in (Mirzaeifar et al., 2013). Other parameters in the above expression are given in the Table 1.

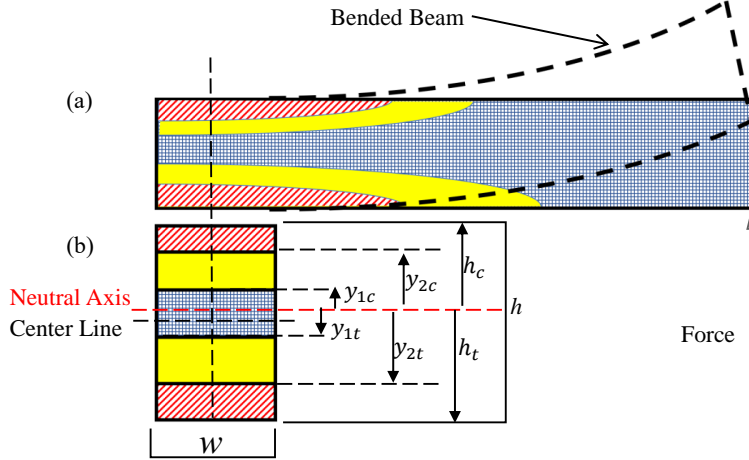


Figure 10: Phase distribution of a Nitinol beam under bending.; (a) phase distribution, blue (meshed), yellow (solid) and red (dashed) are respectively, Austenite, Transition and Martensite Phases; (b) Cross section stress distribution.

---

|   |         |
|---|---------|
| Stainless Steel Stents                        |         |
| Elastic modulus                               | 193 GPa |
| Poisson ratio                                 | 0.3     |
| Uni-axial yield stress                        | 260 MPa |
|   |         |
| Nitinol Stents (Bandyopadhyay and Bose, 2013) |         |
| $E^A$   | 72 GPa  |
| $E^M$   | 30 GPa  |
| Poisson ratio                                 | 0.42    |
| $H^c$   | -0.035  |

---

Table 1: Material properties for the stents used in this study.